

# A Broadband Light-Trapping Nanostructure for InGaP/GaAs Dual-Junction Solar Cells Using Nanosphere Lithography-Assisted Chemical Etching

Shang-Hsuan Wu, Gabriel Cossio, Daniel Derkacs, and Edward T. Yu\*

III–V-based multijunction solar cells have become the leading power generation technology for space applications due to their high power conversion efficiency and reliable performance in extraterrestrial environments. Thinning down the absorber layers of multijunction solar cells can considerably reduce the production cost and improve their radiation hardness. Recent advances in ultrathin GaAs single-junction solar cells suggest the development of light-trapping nanostructures to increase light absorption in optically thin layers within III–V-based multijunction solar cells. Herein, a novel and highly scalable nanosphere lithography-assisted chemical etching method to fabricate light-trapping nanostructures in InGaP/GaAs dual-junction solar cells is studied. Numerical models show that integrating the nanostructured  $\text{Al}_2\text{O}_3/\text{Ag}$  rear mirror significantly enhances the broadband absorption within the GaAs bottom cell. Results demonstrate that the light-trapping nanostructures effectively increase the short-circuit current density in GaAs bottom cells from  $14.04$  to  $15.06 \text{ mA cm}^{-2}$ . The simulated nanostructured InGaP/GaAs dual-junction structure shows improved current matching between the GaAs bottom cell and the InGaP top cell, resulting in  $1.12\times$  higher power conversion efficiency. These findings highlight the potential of light-trapping nanostructures to improve the performance of III–V-based multijunction photovoltaic systems, particularly for high-efficiency applications in space.

the broad solar spectrum with reduced thermal losses.<sup>[1–4]</sup> Among different semiconductor materials, III–V compound semiconductors are preferred in multijunction solar cells due to their outstanding optoelectronic properties such as direct bandgap, high absorption coefficient, tunable optical bandgap by compositional variation of ternary compounds, and high radiation hardness. These superior optoelectronic properties enable III–V multijunction solar cells to harvest the broad solar spectrum, thus leading to a high conversion efficiency of over 30% under unconcentrated solar illumination.<sup>[5]</sup> III–V multijunction cells, particularly inverted metamorphic multijunction (IMM) solar cells,<sup>[6]</sup> have emerged as the dominant technology for photovoltaic (PV) systems powering satellites and spacecraft. However, the harsh conditions of outer space, including exposure to extraterrestrial radiation, pose challenges to the efficiency, performance, and reliability of space PV arrays. The high-energy protons and electrons from the Earth's radiation belts and cosmic rays bombard the solar cells, leading

## 1. Introduction


Multijunction solar cells provide greater power conversion efficiency than single-junction cells by harvesting photons from

to degradation over time.<sup>[7]</sup> These energetic particles cause the displacement of atoms within the crystal lattice of semiconductor material, thus creating defect states and increasing the number of recombination centers. The presence of radiation-induced defects adversely affects the performance of the solar cells due to the decreased minority carrier diffusion lengths and degraded charge carrier collection efficiency. To mitigate the detrimental effects of radiation-induced defects, thinning the absorber layers of solar cells has been proposed as a strategy.<sup>[8]</sup> Thinner absorber layers minimize the diffusion length required for carriers to travel through the material, thereby limiting the impact of defects on carrier transport and improving the radiation tolerance of the solar cells. It has been reported that GaAs solar cells with an 80 nm absorber layer thickness showed no degradation in short-circuit current under high radiation exposure ( $10^{14} \text{ p}^+ \text{ cm}^{-2}$ ) as compared to 74% degradation in short-circuit current density ( $J_{sc}$ ) for an 800 nm absorber layer.<sup>[9]</sup> Radiation exposure data showed thicker GaAs layers in solar cells are more susceptible to radiation-induced defects in geostationary orbit, leading to significant performance degradation.<sup>[10–13]</sup> Moreover, thickness reduction in the absorber layer increases the power-to-weight ratio for space

S.-H. Wu, G. Cossio, E. T. Yu  
Microelectronics Research Center  
Chandra Family Department of Electrical and Computer Engineering  
The University of Texas at Austin  
Austin, TX 78758, USA  
E-mail: ety@ece.utexas.edu

G. Cossio, E. T. Yu  
Center for Dynamics and Control of Materials  
The University of Texas at Austin  
Austin, TX 78712, USA

D. Derkacs  
SolAero Technologies Inc.  
Albuquerque, NM 87123, USA

 The ORCID identification number(s) for the author(s) of this article can be found under <https://doi.org/10.1002/solr.202400531>.

DOI: 10.1002/solr.202400531

PV arrays and leads to considerable savings in material costs and epitaxial processing time.

However, thinner absorber layers will suffer from reduced absorption of incident photons near the band edge, resulting in lower  $J_{sc}$ . This incomplete absorption can be mitigated by implementing effective light-trapping schemes to suppress surface reflection loss and increase the optical path length within the absorber layer.<sup>[14,15]</sup> In recent years, significant progress has been made in developing light-trapping strategies for ultrathin single-junction GaAs solar cells to enhance photogenerated current. However, direct texturization of the absorber layer itself may introduce defects and increase nonradiative recombination, which can offset the benefits of increased light absorption. To address this challenge, alternative light-trapping schemes involve nanotextured surfaces in window layers<sup>[16,17]</sup> and rear surface reflectors<sup>[18–21]</sup> for ultrathin GaAs solar cells. Effective implementation of light-trapping designs can yield a comparable photogenerated current to the conventional optically thick GaAs solar cells, despite using thinner GaAs layers. Chen et al. obtained a remarkable 19.9% efficiency for an ultrathin solar cell based on a 205-nm-thick GaAs absorber combined with a nanostructured Ag rear mirror fabricated by soft nanoimprint lithography.<sup>[22]</sup> Sayre et al. demonstrated a rear surface nanophotonic grating to increase light absorption for an 80 nm GaAs solar cell via the displacement Talbot lithography method.<sup>[23]</sup> While many of these approaches effectively increase the absorption in the ultrathin GaAs solar cells, they often rely on expensive fabrication methods such as photolithography or nanoimprint lithography. This limitation hinders the cost-effectiveness and scalability of the process for wafer-scale cells. Moreover, although significant efforts have been directed toward developing nanotextured light-trapping systems for GaAs single-junction solar cells, their integration into III–V compound multijunction solar cells remains limited. This gap underscores the need for a well-designed light-trapping scheme that can simultaneously achieve high conversion efficiency and reduce the cost of monolithic epitaxy for III–V multijunction solar cells.

In this study, we design and demonstrate a wafer-scale broadband light-trapping nanostructure for InGaP/GaAs dual-junction solar cells fabricated using nanosphere lithography (NSL)-assisted chemical etching. NSL enables rapid, low-cost fabrication of submicrometer nanopatterns via the self-assembled formation of a hexagonal-close-packed (HCP) monolayer of nanospheres, which serves as a patterning mask.<sup>[24]</sup> It provides a scalable and high-throughput lithography process that can be implemented for both rigid and flexible substrates.<sup>[25,26]</sup> In this fabrication approach, 500 nm polystyrene nanospheres were used to pattern a SiO<sub>2</sub> etch mask, and a periodic nanohole pattern was then formed by anisotropic wet chemical etching of the *p*-type AlGaAs back surface field (BSF) layer. A periodic light-trapping Al<sub>2</sub>O<sub>3</sub>/Ag nanostructure array is then integrated with an InGaP/GaAs dual-junction solar cell to induce significantly increased absorption in the GaAs layer via a combination of Fabry–Perot and guided-wave resonances, consequently increasing photocurrent density associated with light absorption in the GaAs bottom cell. The light-trapping Al<sub>2</sub>O<sub>3</sub>/Ag nanostructure is optimized via numerical modeling. As a result, the nanostructured device achieves higher external quantum efficiency at long wavelengths and a corresponding improvement in short circuit

current density, from 14.04 to 15.06 mA cm<sup>−2</sup>. This improvement is due to increased current density associated with the lower (GaAs) subcell and consequently improved current matching. Our simulation results showed a 1.12x higher power conversion efficiency under AM0 illumination, for nanostructured InGaP/GaAs dual-junction solar cells compared to planar InGaP/GaAs dual-junction solar cells. An InGaP/GaP test cell structure fabricated using readily scalable patterning approaches yielded a 1.07x increase in measured short-circuit current density under simulated AM0 illumination. These results indicate that light-trapping structures that can be fabricated without expensive lithographic patterning offer great promise for improving current matching in multijunction solar cells with the potential for direct application in III–V-based multijunction PV systems for space applications.

## 2. Results and Discussion

### 2.1. The Light-Trapping Scheme

Multijunction III–V compound solar cells, composed of distinct semiconductor subcells with different bandgaps, harness the broad spectrum of solar radiation with reduced thermal losses compared to single-junction solar cells, thereby offering enhanced power conversion efficiency.<sup>[27,28]</sup> For multijunction solar cells, the subcells are connected in series through tunnel junctions. Therefore, current matching between the top and bottom cells is critical for optimizing device performance. Finding the optimal thickness of each subcell is crucial to maximizing optical power conversion by balancing light absorption and carrier extraction, as excessively thick layers can lead to increased carrier recombination, and extremely thin layers may limit light absorption.<sup>[29,30]</sup> Similarly, subcell thickness optimization is critically important for real-world implementation because while thicker subcells may increase optical absorption, they also increase manufacturing, decrease radiation hardness, and lower manufacturing throughput, thus negatively impacting commercial viability. Implementing a light-trapping nanostructure to increase optical absorption in the GaAs layer can improve current matching between the InGaP and GaAs subcells while minimizing manufacturing costs and increasing radiation hardness. A schematic light-trapping design for InGaP/GaAs dual-junction solar cells, along with a more conventional structure in which only a planar metal back reflector is present, is shown in **Figure 1**. The planar device structure (Figure 1a) with a back Ag mirror relies on specular reflection to redirect photons back into the GaAs absorber layer; however, a significant portion of incident light may be lost due to incomplete absorption. By strategically incorporating periodic Al<sub>2</sub>O<sub>3</sub> nanostructures into the AlGaAs BSF layer, significant absorption enhancement can be achieved via coupling of incoming light to optical waveguide modes, wherein incident photons are effectively trapped and scattered into the semiconductor absorber layers (Figure 1b). In terms of the circular-hole geometry, it is the most accessible lithographic pattern that can be created in the NSL method. While the other nanostructures, such as pyramidal or rectangular arrays, could offer different or enhanced light-trapping effects,<sup>[15,31]</sup> the circular-hole design was selected based on a

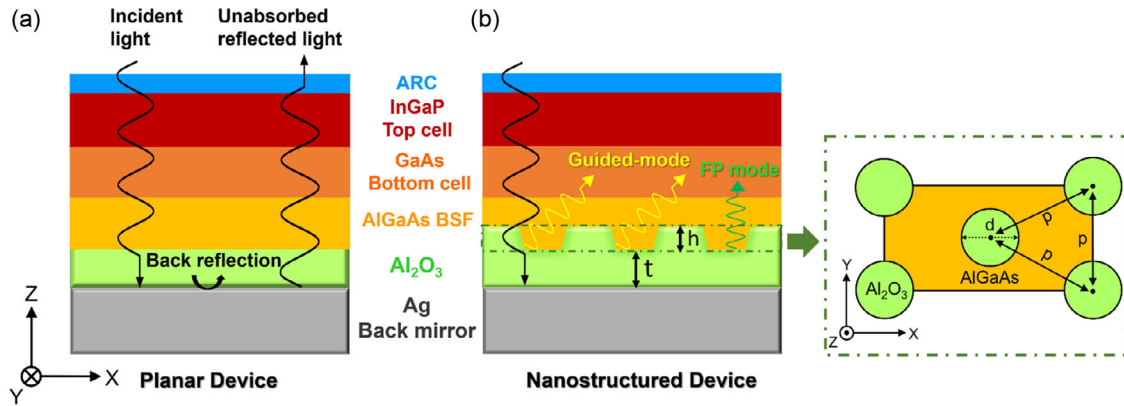


**Figure 1.** Schematics of InGaP/GaAs dual-junction solar cells with a) a planar  $\text{Al}_2\text{O}_3/\text{Ag}$  back reflector and b) nanostructured  $\text{Al}_2\text{O}_3/\text{Ag}$  light-trapping design. The grating geometry parameters of pitch ( $p$ ), diameter ( $d$ ), height ( $h$ ), and the spacer thickness ( $t$ ) are labeled in the figure.

combination of fabrication feasibility, scalability, and proven effectiveness in enhancing light absorption.<sup>[23]</sup> These waveguide modes enable the GaAs bottom cell, in particular, to capture longer wavelengths of sunlight, which are generally inefficiently absorbed. The  $\text{Al}_2\text{O}_3$  nanostructures facilitate incident photons to couple to waveguide modes, which act to trap the light in horizontally propagating modes, which enable a high optical path length within the GaAs absorber layer, increasing the photocurrent to match that generated by the InGaP top cell and ensuring that both junctions contribute equally to the overall photocurrent. This balanced current generation is essential for maximizing the power output and overall performance of InGaP/GaAs dual-junction solar cells.

## 2.2. Optical Modeling for Light-Trapping Structures

The potential performance of light-trapping structures for current matching was determined via optical simulations based on the rigorous coupled-wave analysis method. Our device

design employs two structures: first, an  $\text{Al}_2\text{O}_3$  dielectric spacer is placed between the metallic back contact and the BSF layer. Second, a periodic hexagonal array of nanostructures is incorporated into the BSF layer. The  $\text{Al}_2\text{O}_3$  dielectric spacer acts to limit parasitic optical absorption in the metallic back contact due to the excitation of nonradiative plasmonic resonances. The periodic nanostructure acts as a dielectric grating to provide the necessary in-plane momentum for poorly absorbed long wavelength photons to couple into optical guided modes and as a scattering surface to increase the optical path length within the GaAs subcell. Commercially available software (RSoft, DiffractMod) was used to scan and optimize the design and fabrication-relevant variables, including the grating pitch, grating diameter, dielectric spacer thickness, and grating height. The inset of Figure 1b (green dotted line) outlines the relevant geometric variables, optical materials, and hexagonal unit cell structure utilized in our computational models.

As shown in Figure 2a, optical modeling was performed on nanostructures with different periodicities to find the maxima for optical absorption within the GaAs subcell over its relevant

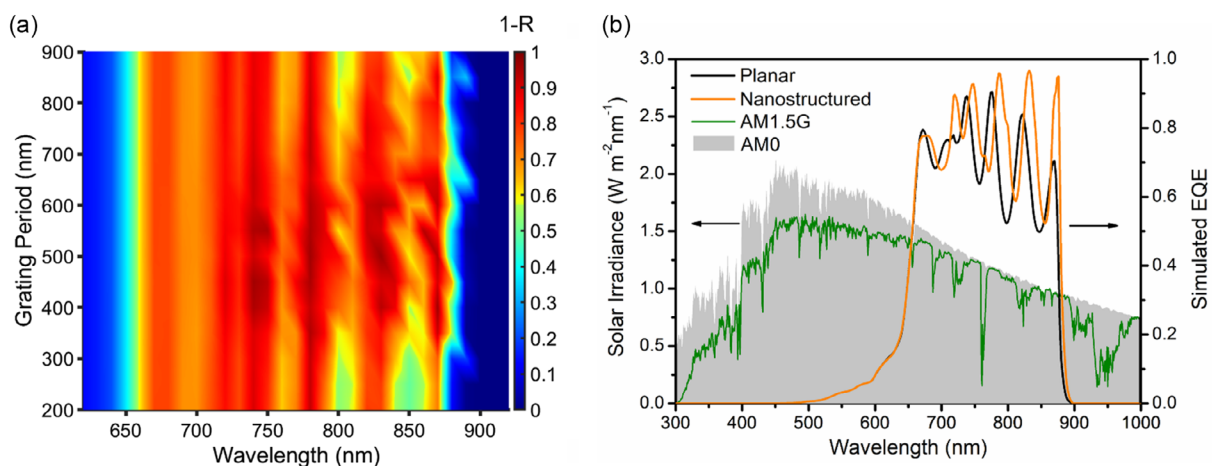


**Figure 2.** a) Simulated optical absorption ( $1-R$ ) in GaAs layer as a function of incident wavelength (620–920 nm) and nanostructured grating period (200–900 nm), with  $d = 250$  nm,  $h = 100$  nm, and  $t = 350$  nm. b) AM1.5G/AM0 solar irradiance and simulated EQE spectra of GaAs bottom cells for planar, and nanostructured device structures.

wavelength range (600–900 nm). The ideal grating period for enhanced light absorption in the GaAs layer is 400–600 nm. Due to the availability of nanosphere sizes from commercial products (Polysciences Inc.), a periodicity of 500 nm was chosen for device processing. Based on the simulation results, we determined the optimal parameters for our light trapping design to be grating pitch ( $p$ ) of 500 nm, grating diameter ( $d$ ) of 250 nm, grating height ( $h$ ) of 100 nm. The spacer thickness ( $t$ ) of 350 nm was selected based on a comprehensive thickness scan ranging from 0 to 900 nm, which indicated that 350 nm provides optimal absorption (see Figure S1, Note S1, Supporting Information). Further increasing the spacer thickness beyond this value did not result in higher absorption. These specific dimensions were chosen to balance the trade-offs between enhanced light absorption and the feasibility of fabrication. Figure 2b shows the simulated optical absorption from a conventional planar device structure (no dielectric spacer, no grating structure) and the nanostructured device with the dielectric spacer and 500 nm period grating. The nanostructured device with the added dielectric spacer and grating (orange line) shows significantly increased absorption at wavelengths longer than 700 nm relative to the planar device (black line). Specifically, the planar device has an average absorption of 62% over the long-wavelength range (700–900 nm), while the nanostructured cell showed a significantly higher average absorption of 70%. This enhancement is attributable to the increased optical path length of incident light within the absorber layer, multiple reflections, and scattering events induced by the nanostructures, particularly at longer wavelengths. The increase in optical absorption then also leads to a corresponding increase in short-circuit current density. To estimate the short-circuit current density ( $J_{sc}$ ) of planar and nanostructured devices under AM 1.5G and AM0 illumination, we calculate  $J_{sc}$  based on the equation<sup>[23]</sup>

$$J_{sc, \text{GaAs(InGaP)}} = e \int_{300\text{nm}}^{1000\text{nm}} \Phi(\lambda) \text{EQE}_{\text{GaAs(InGaP)}}(\lambda) d\lambda \quad (1)$$

where  $e$  is the elementary charge,  $\Phi$  is the photon flux per nm in the AM1.5G or AM0 spectrum, and external quantum efficiency ( $\text{EQE}_{\text{GaAs(InGaP)}}(\lambda)$ ) is the external quantum efficiency associated with the GaAs or InGaP absorber layer as a function of wavelength. The  $J_{sc, \text{GaAs(InGaP)}}$  can thereby be calculated separately for the GaAs and InGaP subcells. The wavelength range was chosen to be between 300 and 1000 nm based on the bandgaps of InGaP and GaAs (1.90 and 1.42 eV, respectively). Unless otherwise specified, the optical power was normally incident on the solar cell structure and was 45° polarized. Based on the simulated EQE spectra of the GaAs bottom cell in Figure 2b, we see that the expected  $J_{sc}$  for the nanostructured GaAs bottom cell was enhanced by 12.3%, from 11.78 to 13.23 mA cm<sup>-2</sup> under AM1.5G, and 12.1%, from 13.11 to 14.70 mA cm<sup>-2</sup>, under AM0 as compared to the planar GaAs bottom cell (Table 1). Notably, while the GaAs bottom cell demonstrates enhanced absorption in the presence of nanostructures, the EQE spectra of the InGaP top cell remain unchanged between the planar and nanostructured devices (see Figure S2, Supporting Information).  $J_{sc}$  values calculated based on the simulated EQE spectra of the InGaP top cell were 14.30 and 18.22 mA cm<sup>-2</sup> under AM1.5G and AM0 illumination,

**Table 1.** Calculated  $J_{sc}$  values of GaAs bottom cells with planar and nanostructured Al<sub>2</sub>O<sub>3</sub>.

Device	Calculated $J_{sc}$ under AM1.5G [mA cm <sup>-2</sup> ]	Calculated $J_{sc}$ under AM0 [mA cm <sup>-2</sup> ]
Planar GaAs cell	11.78	13.11
Nanostructured GaAs cell	13.23	14.70

respectively. This is due to the high optical absorption efficiency of InGaP within this wavelength range (300–1000 nm) and the InGaP layer being sufficiently optically thick (600 nm). These results demonstrate the great potential of light trapping as an approach to improve current matching, and thereby overall power conversion efficiency, in InGaP/GaAs dual-junction and potentially other multijunction solar cells.

To further elucidate the mechanisms of the increased optical absorption in the nanostructured cell, the simulated electric field profiles within the two cells were analyzed. Figure 3 shows the electric field components within the different cells when illuminated at a wavelength of 870 nm. This wavelength was chosen since both the planar and nanostructured cells share an absorption peak at 870 nm. Therefore, any changes in the electric field profiles may help explain the large increase in absorption efficiency of the nanostructured cell relative to the planar cell. From Figure 3a–c, it can be seen that the planar cell does not support electric fields with an  $E_z$  component under 870 nm illumination, while the  $E_x$  and  $E_y$  components show oscillatory behavior. This oscillating electric field profile is reminiscent of a Fabry–Perot resonance, which arises from the interference of vertically traveling waves after partially reflecting from the refractive index discontinuities in the semiconductor stack. In contrast to the unpatterned planar solar cell, the device with the nanostructured cell (Figure 3d–f) shows a complex electric field profile and, importantly, a nonzero  $E_z$  component of the electric field. Since an electric field with a nonzero  $E_z$  component must have a wave vector component that is parallel to the XY plane, the included nanopatterned grating is horizontally scattering long-wavelength photons into guided-wave modes within the semiconductor absorber layers. The horizontally scattered photons also have an enhanced optical path length, which increases their probability of absorption. Of particular interest, the enhanced current generation from the nanostructured cell persists at all angles of incidence (Figure S3, Note S2, Supporting Information), which further demonstrates the capacity for light trapping to provide power generation benefits in various applications which may be severely hampered by Fresnel reflection loss, such as emerging building integrated and automobile integrated PV.

## 2.3. Experimental Demonstration

### 2.3.1. Device Fabrication

Based on the numerical model, a light-trapping nanostructure with a 500 nm periodic pattern in the AlGaAs BSF layer provides optimal enhancement of broadband absorption in the GaAs

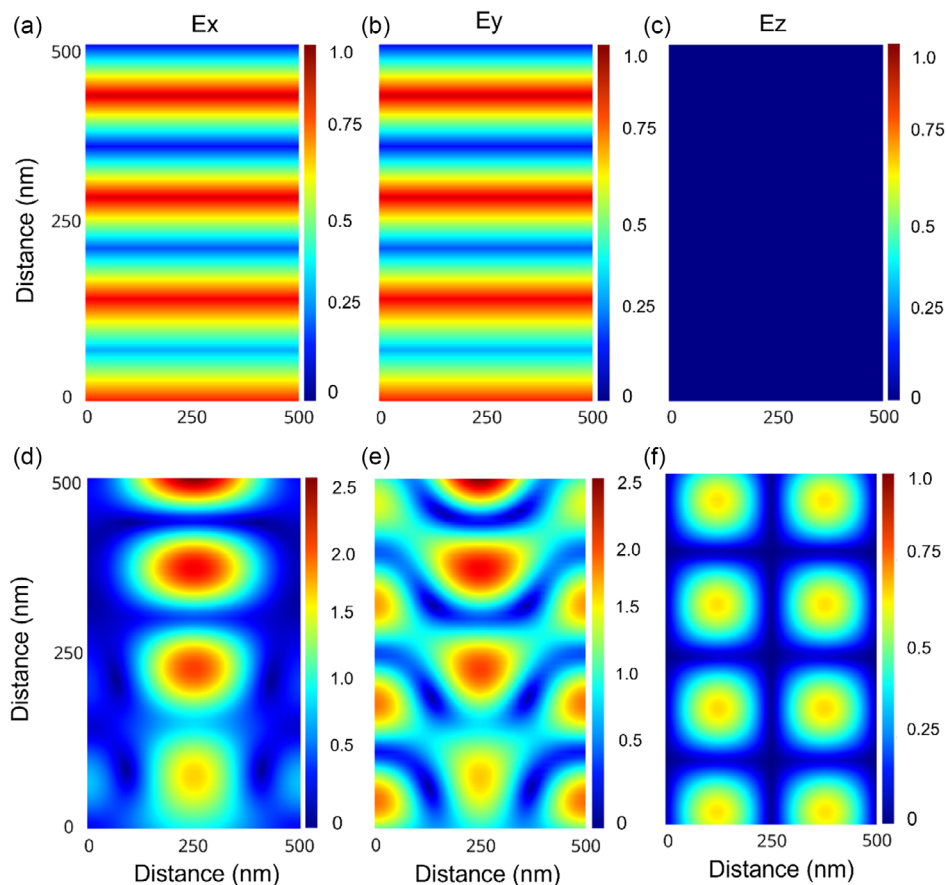


**Figure 3.** Electric field components in GaAs cells illuminated at a wavelength of 870 nm in in-plane (Ex), in-plane (Ey), and out-of-plane (Ez) directions. a) Ex, b) Ey, and c) Ez fields of GaAs cells with planar structure. d) Ex, e) Ey, and f) Ez fields of GaAs cells with light-trapping structure.

bottom cell by coupling incoming light to both Fabry–Perot and guided-wave resonances. The simulated EQE spectra of the InGaP top cell showed an unchanged absorption for the planar and nanostructured devices. Therefore, a simplified InGaP/GaAs isotype structure comprising a 600 nm InGaP filter and 500 nm GaAs absorber was prepared to study the light-trapping contribution to the GaAs bottom cells. The epitaxial layers were grown by metal-organic chemical vapor deposition (MOCVD) on a GaAs substrate in an inverted configuration with rear side grown last. A detailed description of the epitaxial layers is provided in Table S1, Supporting Information. **Figure 4** shows a schematic of the fabrication process for NSL-assisted chemical etching to create light-trapping nanostructures integrated with the InGaP/GaAs isotype structure. A 4 inch InGaP/GaAs isotype wafer was first prepared and transferred to a drop-cast station for 500 nm polystyrene NSL using the same approach from our previous work.<sup>[32]</sup> Briefly, the colloidal solution containing polystyrene nanospheres was injected via a pipette tip to the air–water interface of an aqueous reservoir and formed a HCP monolayer. The self-assembled HCP nanospheres were then deposited onto the InGaP/GaAs isotype wafer by draining the reservoir and air drying overnight at room temperature. Next, the NSL-patterned wafer was processed with an O<sub>2</sub> plasma etch using reactive ion etching (RIE) to reduce the diameter of the nanospheres to

100 nm. Next, a 15 nm SiO<sub>2</sub> hard mask layer was deposited using electron beam evaporation. The nanospheres were lifted off to form a nanopattern in the remaining SiO<sub>2</sub>, which served as a mask for a sequential wet etch process. Selective etching of the 500 nm AlGaAs BSF layer was carried out for 75 secs using a citric acid/H<sub>2</sub>O<sub>2</sub> solution<sup>[33,34]</sup> consisting of 120 g citric acid monohydrate mixed in 120 mL DI water and 15 mL 30% H<sub>2</sub>O<sub>2</sub>. After achieving the desired etch depth of 100–150 nm, the SiO<sub>2</sub> hard mask was removed by a buffered oxide etch. Al<sub>2</sub>O<sub>3</sub> (350 nm) and Ag (5000 nm) were then deposited sequentially by e-beam evaporation. The isotype wafer was inverted 180°, and the Ag back surface was bonded to a rigid handling substrate coated with a low outgassing adhesive. Next, the GaAs growth substrate was mechanically thinned and chemically etched, stopping on the InGaP etch stop. Finally, HCl etching exposed the cap layer of the InGaP/GaAs isotype structure. The standard Ag-based front contact grid was deposited after the InGaP etch stop was removed. The GaAs cap was then chemically removed, exposing the InGaP filter layer, and coated with an e-beam-deposited two-layer TiO<sub>2</sub>/Al<sub>2</sub>O<sub>3</sub> antireflection coating. The wafer was mesa isolated, resulting in 12 cells wafer<sup>-1</sup>, each having a physical cell area of 4.02 cm<sup>2</sup>. The wafer was thermally annealed to promote ohmic contact formation and metal adhesion.

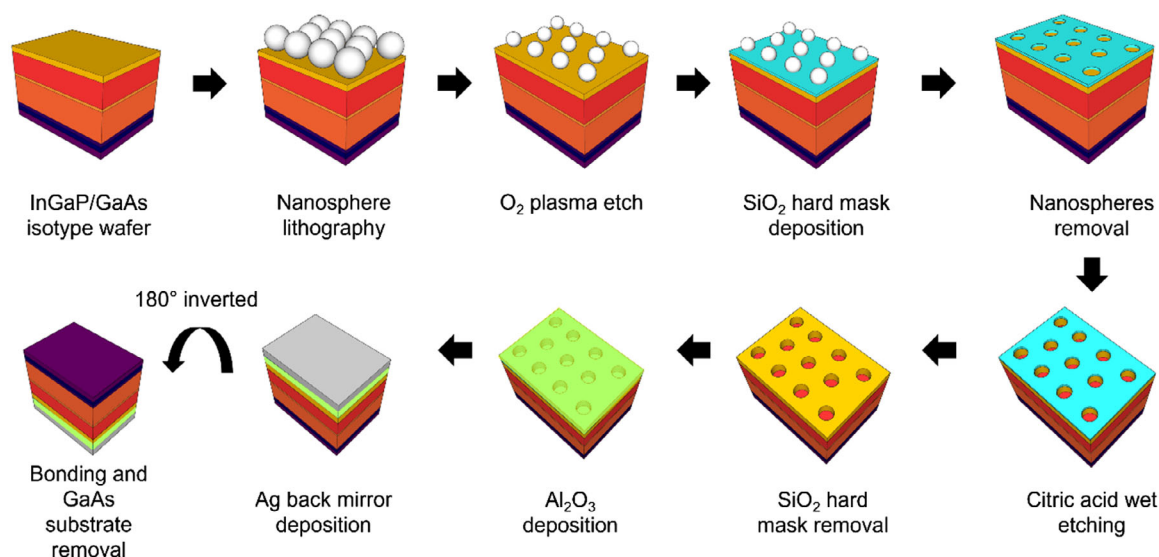


**Figure 4.** The fabrication process for dual-junction InGaP/GaAs solar cells incorporating a nanostructured  $\text{Al}_2\text{O}_3/\text{Ag}$  rear mirror.

To further investigate the NSL-assisted chemical wet etching process and the resulting surface morphology, we performed scanning electron microscopy (SEM) and atomic force microscopy (AFM) to characterize the etched AlGaAs BSF layer. **Figure 5a** shows an SEM image exhibiting a typical periodic pattern with an average hole diameter of  $\approx 200$  nm created in the AlGaAs BSF layer after 75 s of etching in citric acid/ $\text{H}_2\text{O}_2$  solution at room temperature. The AFM image in **Figure 5b** shows a similar average hole diameter of  $\approx 200$  nm, and the corresponding AFM height profile in **Figure 5c** gives an average hole depth of  $\approx 120$  nm. The etched hole structures showed uniform size and spacing, which can be attributed to high-quality nanosphere monolayer formation combined with good optimization of the  $\text{O}_2$  etching process for the polystyrene nanospheres and subsequent  $\text{SiO}_2$  etch mask formation (see **Figure S4a,b**, Supporting Information). Our previous work has proven that the PS nanosphere monolayer can form large single-crystal domains ( $>2300 \mu\text{m}^2$ ) and exhibit long-range order across a  $158 \text{ cm}^2$  substrate area.<sup>[26]</sup> While there are various point and line defects in the self-assembled nanosphere arrays, these defects are deeply subwavelength and thus do not efficiently scatter the light in

the wavelength of interest. The undercut feature beneath the  $\text{SiO}_2$  etch mask was observed during the wet etch process, and it becomes more pronounced as the etch time increases (see **Figure S4c,d**, Supporting Information), leading to over-etched hole dimensions and compromising the structural integrity of the features. To mitigate this issue and ensure precise control over the etched hole diameter size, we optimized a shorter etch time (75 s). The NSL-assisted chemical wet etch enables precise control in periodic nanostructures over a 4-inch wafer (see **Figure S5**, Supporting Information). We note that the fabrication processes employed here are all relatively fast and low cost and that the RIE step has the potential to be replaced by alternate etch processes, for example,  $\text{O}_2$  plasma etching in a photoresist ash<sup>[35]</sup> or by deposition of core-shell nanoparticles followed by a wet etch.<sup>[26]</sup>

### 2.3.2. Device Performance and Analysis

**Figure 6a** shows the measured  $J-V$  characteristics of the best-performing planar and nanostructured GaAs bottom cells under

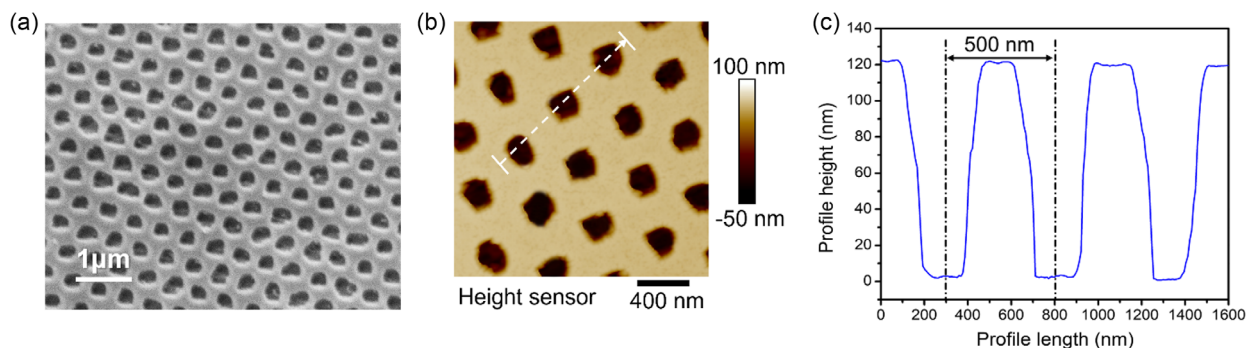


**Figure 5.** Surface morphology of the NSL-assisted chemical wet etched AlGaAs BSF layer. a) SEM image. b) AFM image with c) corresponding height profile.

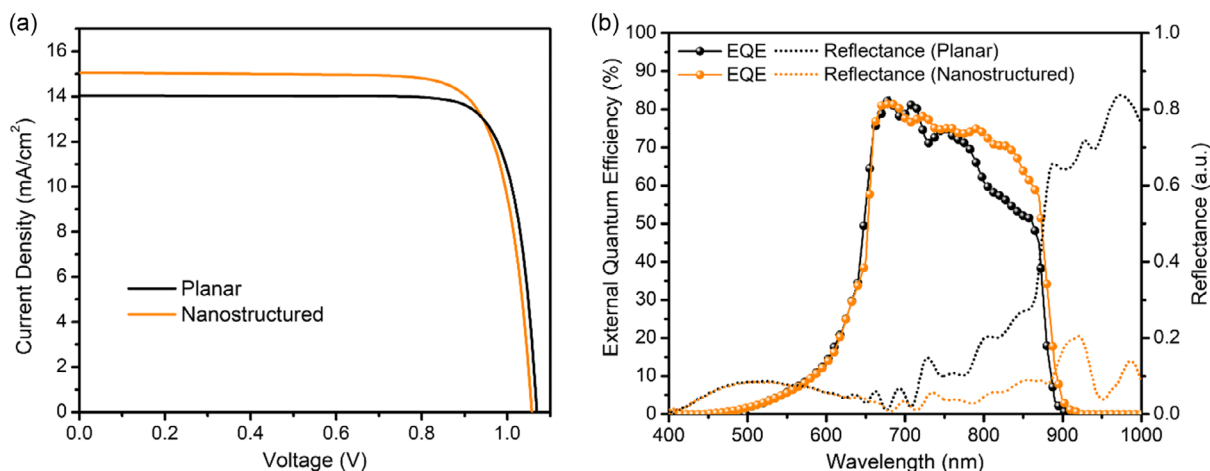


**Figure 6.** a)  $J$ - $V$  characteristics and b) External quantum efficiency and specular reflectance spectra of planar and nanostructured GaAs bottom cells under AM0 illumination.

AM0 illumination. The additional  $J$ - $V$  and EQE data sets provided in Figure S6, Supporting Information, consistently demonstrate improvements in  $J_{sc}$  values and spectral response across all nanostructured devices. The PV parameters of devices are summarized in Table 2. Notably, the nanostructured GaAs bottom cell exhibits distinct improvement in  $J_{sc}$  15.06 mA cm<sup>-2</sup> compared to 14.04 mA cm<sup>-2</sup> for the planar GaAs bottom cell. The increased  $J_{sc}$  can be ascribed to the effective light trapping and enhanced absorption from the nanostructure. However, despite the increased  $J_{sc}$ , the open-circuit voltage ( $V_{oc}$ ) and fill factor (FF) in the nanostructured GaAs bottom cell exhibit slight decreases, from 1.07 to 1.05 V and 82.2% to 79.5%, respectively. The shunt resistance ( $R_{SH}$ ) is fit based on the slope  $(dJ/dV)^{-1}$  of the corresponding  $J$ - $V$  curves at  $J_{sc}$ . We found that the nanostructured device has a lower  $R_{SH}$  of  $1.74 \times 10^3 \Omega$  as compared to the planar device of  $6.37 \times 10^4 \Omega$ . We attributed the lower  $V_{oc}$  and FF in the nanostructured device to underetching during the mesaisolation process. During this process, underetching can inadvertently create unintended conductive paths at the edges of the nanostructured areas, leading to a reduction in the overall  $R_{SH}$  of the device. A lower  $R_{SH}$  causes leakage currents that divert current from the main junction, thereby reducing both  $V_{oc}$  and FF.<sup>[36,37]</sup> Nevertheless, the power conversion efficiency (PCE) of the nanostructured device improves from 9.03% to 9.22%. The increased  $J_{sc}$  in the nanostructured device is consistent with the enhancement in EQE (see Figure 6b). Specifically, the nanostructured device exhibits a higher spectral response in the longer wavelength range from 700 to 900 nm than the planar device, which coincides with

our simulated EQE results in Figure 2b. The slight discrepancy ( $\approx 5\%$ ) between the integrated  $J_{sc}$  from EQE and  $J_{sc}$  obtained from the  $J$ - $V$  curve most likely originates from the mismatched external quantum efficiency of the optically thick isotypes used to calibrate the solar simulator and the external quantum efficiency of the optically thin devices discussed herein.<sup>[38]</sup> The specular reflectance spectra in Figure 6b show a significant difference between the nanostructured and planar devices, with the nanostructured device exhibiting markedly lower reflectance across the measured wavelengths. This reduction in reflectance highlights the effective light-trapping capabilities of the nanostructures. By incorporating nanostructures, the incident light is scattered into the semiconductor absorber layers rather than being reflected away, thereby enhancing the optical path length within the device. This increased optical path length boosts the photon absorption, leading to a greater generation of electron-hole pairs and, subsequently, higher photocurrent. The enhanced light-trapping effect of the nanostructured device, as evidenced by the higher  $J_{sc}$  and reduced reflectance, underscores its potential to improve the overall efficiency of solar cells by maximizing the utilization of the incident solar spectrum and, in a multijunction solar cell, allowing for improved current matching.

To further evaluate the performance of InGaP/GaAs dual-junction solar cells with light-trapping nanostructures, simulations of the  $J$ - $V$  curves for both planar and nanostructured devices were computed assuming that each subcell behaves as an ideal diode (details included in Note S3, Supporting Information) with zero series resistance. Figure 7 shows the simulated  $J$ - $V$  curves of planar and nanostructured GaAs bottom

**Table 2.** PV parameters of the best planar and nanostructured GaAs bottom cells.

Device	$J_{sc}^a$ [mA cm <sup>-2</sup> ]	$J_{sc}^b$ [mA cm <sup>-2</sup> ]	$V_{oc}$ [V]	FF [%]	PCE [%]	$R_{SH}$ [ $\Omega$ ]
Planar GaAs cell	14.04	13.39	1.07	82.2	9.03	$6.37 \times 10^4$
Nanostructured GaAs cell	15.06	14.33	1.05	79.5	9.22	$1.74 \times 10^3$

<sup>a</sup>) Measured  $J_{sc}$  values from  $J$ - $V$  curves under AM0 solar simulator; <sup>b</sup>) Integrated  $J_{sc}$  values from the EQE measurement.

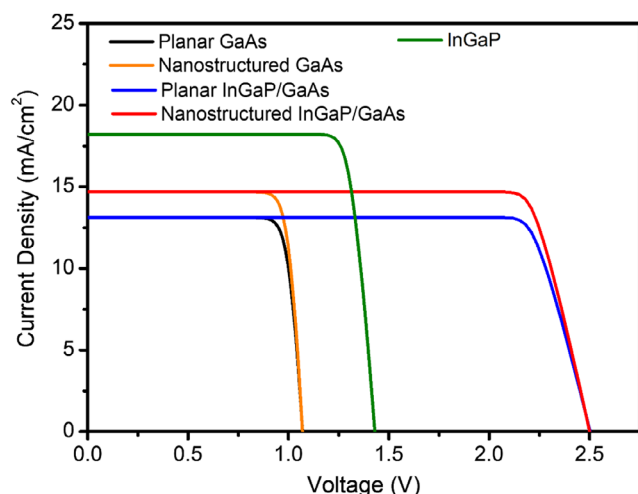


**Figure 7.** Simulated  $J$ - $V$  curves of planar and nanostructured GaAs bottom cells, InGaP top cell, and planar and nanostructured InGaP/GaAs dual junctions under AM0 illumination.

**Table 3.** Simulated PV parameters of the planar and nanostructured GaAs bottom cells and InGaP/GaAs dual junctions under AM0 illumination.

Device	$J_{sc}$ [ $\text{mA cm}^{-2}$ ]	$V_{oc}$ [V]	FF [%]	PCE [%]
Planar GaAs cell	13.11	1.07	85.0	8.73
Nanostructured GaAs cell	14.70	1.07	85.0	9.79
InGaP cell	18.21	1.43	85.0	16.22
Planar InGaP/GaAs dual junction	13.11	2.50	85.0	20.39
Nanostructured InGaP/GaAs dual junction	14.70	2.50	85.0	22.87

cells, InGaP top cells, and planar and nanostructured InGaP/GaAs dual junctions under AM0 illumination. The simulated PV parameters of devices are summarized in **Table 3**. For GaAs bottom cells with an ideal FF (85%) and a fixed  $V_{oc}$  of 1.07 V, the nanostructured device achieves a higher  $J_{sc}$  and PCE of  $14.70 \text{ mA cm}^{-2}$  and 9.79%, respectively, compared to the planar device of  $13.11 \text{ mA cm}^{-2}$  and 8.73%. This represents a 12% improvement in performance. The  $J$ - $V$  curve of the InGaP top cell was simulated with an ideal FF (85%), which showed  $V_{oc}$ ,  $J_{sc}$ , and PCE of 1.43 V,  $18.21 \text{ mA cm}^{-2}$ , and 16.22%, respectively. Finally, the planar and nanostructured InGaP/GaAs dual junctions were simulated, where the  $V_{oc}$  of 2.5 V is defined as the combined value of  $V_{oc}$  of the InGaP top cells (1.43 V) and GaAs bottom cells (1.07 V). Notably, the simulated results indicate that the nanostructured device achieves better current matching with the InGaP top cell, resulting in an enhanced PCE of 22.87% in InGaP/GaAs dual-junction solar cells compared to 20.39% for the cell with a planar back contact.

### 3. Conclusion

In this work, a light-trapping nanostructure is designed to improve long-wavelength light absorption and consequently

current matching for InGaP/GaAs dual-junction solar cells. Our numerical models demonstrate that the integration of periodic  $\text{Al}_2\text{O}_3/\text{Ag}$  nanostructures in the AlGaAs BSF layer produces a strong absorption enhancement for the GaAs bottom cell. The broadband absorption increase in the GaAs layer can be ascribed to a combination of Fabry–Perot and guided-wave resonances into which incident light can be scattered by the  $\text{Al}_2\text{O}_3/\text{Ag}$  nanostructured rear mirror. Notably, the simulations indicate that an increase of 1.12x in power conversion efficiency can be achieved in nanostructured InGaP/GaAs dual-junction solar cells, attributable to improved current matching between the GaAs bottom cells and the InGaP top cells. For experimental demonstration, we have employed a highly scalable NSL-assisted chemical etching method to fabricate light-trapping nanostructures in InGaP/GaAs dual-junction solar cells. Both  $J$ - $V$  and EQE measurements show increased  $J_{sc}$  in nanostructured GaAs bottom cells. This highlights that the NSL approach enables low-cost, large-area implementation of highly effective light-trapping nanostructures in III–V-based multijunction PV systems for space applications.

### 4. Experimental Section

**Epitaxial Growth of Semiconductor Layers:** The III–V semiconductor layers were grown by MOCVD at SolAero Technologies in a Veeco E450 reactor. The layer thicknesses and doping types are provided in Table S1, Supporting Information. The epitaxial growth was conducted on GaAs substrate, consisting of InGaP etch stop, GaAs cap, InGaP filter,  $p^+$  AlGaAs and  $n^+$  InGaP tunnel diodes, InGaP window, 500 nm GaAs homojunction as the main absorber of subcell,  $p^+$  AlGaAs BSF, and  $p^{++}$  GaAs contact layer.

**Fabrication of Nanostructured  $\text{Al}_2\text{O}_3/\text{Ag}$  Rear Mirror:** First, 4 inch GaAs wafers with the epitaxial-grown InGaP/GaAs isotype structure were thoroughly cleaned using a sequential sonication process with acetone, methanol, and deionized water. Then, the wafers were immersed in water in a drop-cast container. 500 nm polystyrene nanospheres were injected at the air–water interface, creating a self-assembled monolayer of spherical particles. After that, the water was drained, allowing the HCP pattern of polystyrene spheres to deposit on the wafers. Then, the wafers were air dried at room temperature for 24 h. Next, the wafers were etched under  $\text{O}_2$  plasma in a reactive ion etcher (Oxford Instruments) to reduce the nanosphere size. Subsequently,  $\text{SiO}_2$  ( $\approx 15 \text{ nm}$ ) was deposited on the wafers using an e-beam evaporator (CHA Industries) with a base chamber pressure of  $5 \times 10^{-6}$  Torr and deposition rate of  $1 \text{ \AA s}^{-1}$ . After that, the polystyrene spheres were lifted off the substrates using a sonication process with toluene for 10 min. The selective etching in the 500 nm AlGaAs BSF layer was carried out using a citric acid/ $\text{H}_2\text{O}_2$  solution, which consisted of 120 g citric acid monohydrate mixed in 120 mL DI water and 15 mL 30%  $\text{H}_2\text{O}_2$ . After 75 s of the citric acid etch at room temperature, the wafers were rinsed with DI water and transferred to a buffered oxide etch for  $\text{SiO}_2$  hard mask removal. Finally, the  $\text{Al}_2\text{O}_3$  (350 nm) and Ag (5000 nm) were e-beam deposited sequentially to form the rear mirror.

**InGaP/GaAs IMM Solar Cell Fabrication:** HCl etching transferred the InGaP/GaAs tandem structure from the GaAs substrate and invertedly bonded it with a glass-handling substrate coated with epoxy. After removing the InGaP etch stop, the front contact grid of Au was deposited. Each device with an area of  $4.02 \text{ cm}^2$  was isolated by mesa etching.

**Device Characterization:** The surface morphology and topography of the nanostructured AlGaAs BSF layer were investigated using SEM (Zeiss Neon 40) and AFM (Bruker Icon), respectively.  $J$ - $V$  measurements were conducted at SolAero Technologies using a TS-Space Systems Unisim 4-zone solar simulator. The solar simulator was calibrated to the AM0 spectrum using balloon-flight-calibrated InGaP and GaAs single-junction isotypes. EQE measurements were conducted in a custom-built QE setup



using a Newport Cornerstone 260 1/4 m monochromator, Stanford Research lock-in amplifier, transimpedance amplifier, and NIST-calibrated Si, InGaAs, and Ge photodetectors. Specular reflectance was measured using a Filmetrics F20 spectrophotometer.

**Optical Modeling:** Simulated EQE (absorption) spectra were carried out with Synopsys, DiffractMOD model, using a 3D model based on planar and nanostructured InGaP/GaAs devices. Periodicity, diameter, and thicknesses of Al<sub>2</sub>O<sub>3</sub> nanostructures were defined as 500, 250, 100 nm, respectively. The background was set to glass ( $n = 1.5$ ), and the refractive index of each epitaxial layer was measured by ellipsometry. The refractive index of the Ag was obtained from DiffractMOD material database.

## Supporting Information

Supporting Information is available from the Wiley Online Library or from the author.

## Acknowledgements

This work was partially supported by NSF award no. CBET-2109842 and by the National Science Foundation through the Center for Dynamics and Control of Materials: an NSF MRSEC under Cooperative Agreement Nos. DMR-1720595 and DMR-2308817. The authors acknowledge the use of facilities and instrumentation supported by the National Science Foundation through the Center for Dynamics and Control of Materials: an NSF MRSEC under Cooperative Agreement Nos. DMR-1720595 and DMR-2308817. This work was performed in part at the University of Texas Microelectronics Research Center, a member of the National Nanotechnology Coordinated Infrastructure (NNCI), which was supported by the National Science Foundation (grant ECCS-2025227).

## Conflict of Interest

The authors declare no conflict of interest.

## Author Contributions

**Shang-Hsuan Wu:** Conceptualization (lead); Data curation (lead); Formal analysis (Lead); Investigation (lead); Methodology (lead); Software (lead); Validation (lead); Visualization (lead); Writing—original draft (lead); Writing—review & editing (lead). **Gabriel Cossio:** Conceptualization (supporting); Data curation (supporting); Formal analysis (supporting); Software (equal); Validation (supporting); Visualization (supporting); Writing—original draft (supporting); Writing—review & editing (supporting). **Daniel Derkacs:** Data curation (lead); Formal analysis (lead); Methodology (lead); Validation (equal); Visualization (equal); Writing—original draft (supporting); Writing—review & editing (supporting). **Edward T. Yu:** Conceptualization (lead); Funding acquisition (lead); Investigation (lead); Methodology (lead); Project administration (lead); Resources (lead); Software (supporting); Supervision (lead); Validation (lead); Visualization (lead); Writing—original draft (equal); Writing—review & editing (lead).

## Data Availability Statement

The data that support the findings of this study are available on request from the corresponding author. The data are not publicly available due to privacy or ethical restrictions.

## Keywords

GaAs, III–V multijunction solar cells, light trapping, multijunction solar cells, nanosphere lithographies

Received: July 18, 2024

Revised: September 11, 2024

Published online:

- [1] M. Yamaguchi, T. Takamoto, A. Khan, M. Imaizumi, S. Matsuda, N. J. Ekins-Daukes, *Prog. Photovoltaics* **2005**, *13*, 125.
- [2] M. S. Leite, R. L. Woo, J. N. Munday, W. D. Hong, S. Mesropian, D. C. Law, H. A. Atwater, *Appl. Phys. Lett.* **2013**, *102*, 033901.
- [3] F. Dimroth, M. Grave, P. Beutel, U. Fiedler, C. Karcher, T. N. D. Tibbits, E. Oliva, G. Siefert, M. Schachtner, A. Wekkeli, A. W. Bett, R. Krause, M. Piccin, N. Blanc, C. Drazek, E. Guiot, B. Ghyselen, T. Salvetat, A. Tauzin, T. Signamarcheix, A. Dobrich, T. Hannappel, K. Schwarzburg, *Prog. Photovoltaics* **2014**, *22*, 277.
- [4] G. Oh, Y. Kim, S. J. Lee, E. K. Kim, *Sol. Energy Mater. Sol. Cells* **2020**, *207*, 110359.
- [5] M. A. Green, E. D. Dunlop, M. Yoshita, N. Kopidakis, K. Bothe, G. Siefert, X. Hao, *Prog. Photovoltaics* **2024**, *32*, 3.
- [6] J. F. Geisz, D. J. Friedman, J. S. Ward, A. Duda, W. J. Olavarria, T. E. Moriarty, J. T. Kiehl, M. J. Romero, A. G. Norman, K. M. Jones, *Appl. Phys. Lett.* **2008**, *93*, 123505.
- [7] M. Ochoa, E. Yacuzzi, P. Espinet-González, M. Barrera, E. Barrigón, M. L. Ibarra, Y. Contreras, J. García, E. López, M. Alurralde, C. Algora, E. Godfrin, I. Rey-Stolle, J. Plá, *Sol. Energy Mater. Sol. Cells* **2017**, *159*, 576.
- [8] I. Massiot, A. Cattoni, S. Collin, *Nat. Energy* **2020**, *5*, 959.
- [9] L. C. Hirst, M. K. Yakes, J. H. Warner, M. F. Bennett, K. J. Schmieider, R. J. Walters, P. P. Jenkins, *Appl. Phys. Lett.* **2016**, *109*, 033908.
- [10] N. Gruginskie, F. Cappelluti, M. van Eerden, G. Bauhuis, P. Mulder, E. Vlieg, J. Schermer, *Sol. Energy Mater. Sol. Cells* **2021**, *223*, 110971.
- [11] E. Yacuzzi, S. Di Napoli, E. J. Di Liscia, S. Suárez, M. Alurralde, A. Strittmatter, J. Pla, P. Giudici, *J. Phys. D: Appl. Phys.* **2021**, *54*, 115302.
- [12] J. Li, A. Aierken, Y. Liu, Y. Zhuang, X. Yang, J. H. Mo, R. K. Fan, Q. Y. Chen, S. Y. Zhang, Y. M. Huang, Q. Zhang, *Front. Phys.* **2021**, *8*, 631925.
- [13] J. M. Raya-Armenta, N. Bazmohammadi, J. C. Vasquez, J. M. Guerrero, *Sol. Energy Mater. Sol. Cells* **2021**, *233*, 111379.
- [14] E. T. Yu, J. van de Lagemaat, *MRS Bull.* **2011**, *36*, 424.
- [15] E. Camarillo Abad, H. J. Joyce, L. C. Hirst, *Opt. Express* **2020**, *28*, 39093.
- [16] S.-M. Lee, A. Kwong, D. Jung, J. Faucher, R. Biswas, L. Shen, D. Kang, M. L. Lee, J. Yoon, *ACS Nano* **2015**, *9*, 10356.
- [17] D. Liang, Y. Kang, Y. Huo, Y. Chen, Y. Cui, J. S. Harris, *Nano Lett.* **2013**, *13*, 4850.
- [18] W. Yang, J. Becker, S. Liu, Y.-S. Kuo, J.-J. Li, B. Landini, K. Campman, Y.-H. Zhang, *J. Appl. Phys.* **2014**, *115*, 203105.
- [19] N. Vandamme, H. L. Chen, A. Gaucher, B. Behaghel, A. Lemaître, A. Cattoni, C. Dupuis, N. Bardou, J. F. Guillemoles, S. Collin, *IEEE J. Photovoltaics* **2015**, *5*, 565.
- [20] M. van Eerden, G. J. Bauhuis, P. Mulder, N. Gruginskie, M. Passoni, L. C. Andreani, E. Vlieg, J. J. Schermer, *Prog. Photovoltaics* **2020**, *28*, 200.
- [21] J. R. D'Rozario, S. J. Polly, G. T. Nelson, S. M. Hubbard, *IEEE J. Photovoltaics* **2020**, *10*, 1681.
- [22] H.-L. Chen, A. Cattoni, R. De Lépinay, A. W. Walker, O. Höhn, D. Lackner, G. Siefert, M. Faustini, N. Vandamme, J. Goffard, B. Behaghel, C. Dupuis, N. Bardou, F. Dimroth, S. Collin, *Nat. Energy* **2019**, *4*, 761.

- [23] L. Sayre, E. Camarillo Abad, P. Pearce, P. Chausse, P.-M. Coulon, P. Shields, A. Johnson, L. C. Hirst, *Prog. Photovoltaics* **2022**, *30*, 96.
- [24] S.-H. Wu, G. Cossio, B. Braun, F. C. M. Wu, E. T. Yu, *Adv. Opt. Mater.* **2023**, *11*, 2202409.
- [25] P. Gao, J. He, S. Zhou, X. Yang, S. Li, J. Sheng, D. Wang, T. Yu, J. Ye, Y. Cui, *Nano Lett.* **2015**, *15*, 4591.
- [26] G. Cossio, R. Barbosa, B. Korgel, E. T. Yu, *Adv. Mater.* **2024**, *36*, 2309775.
- [27] H. Fujii, K. Toprasertpong, Y. Wang, K. Watanabe, M. Sugiyama, Y. Nakano, *Prog. Photovoltaics* **2014**, *22*, 784.
- [28] M. A. Steiner, R. M. France, J. Buencuerpo, J. F. Geisz, M. P. Nielsen, A. Pusch, W. J. Olavarria, M. Young, N. J. Ekins-Daukes, *Adv. Energy Mater.* **2021**, *11*, 2002874.
- [29] A. Razi, A. Safdar, R. Irfan, *Nanomaterials* **2023**, *13*, 2985.
- [30] L. Zhu, Y. Wang, X. Pan, H. Akiyama, *Opt. Express* **2022**, *30*, 35202.
- [31] L. Zhu, Y. Hazama, A. Reddy, K. Watanabe, Y. Nakano, M. Sugiyama, H. Akiyama, *Prog. Photovoltaics* **2020**, *28*, 251.
- [32] G. Cossio, E. T. Yu, *Nano Lett.* **2020**, *20*, 5090.
- [33] G. C. DeSalvo, W. F. Tseng, J. Comas, *J. Electrochem. Soc.* **1992**, *139*, 831.
- [34] J.-H. Kim, D. H. Lim, G. M. Yang, *J. Vac. Sci. Technol., B* **1998**, *16*, 558.
- [35] Y. Chen, D. Shi, Y. Chen, X. Chen, J. Gao, N. Zhao, C. P. Wong, *Nanomaterials* **2019**, *9*, 605.
- [36] I. M. Hamammu, K. Ibrahim, in *Proc. of the 9th Int. Conf. on Neural Information Processing, Computational Intelligence for the E-Age*, Penang, Malaysia, December **2002**.
- [37] M. Raappana, T. Koikkalainen, V. Polojärvi, A. Aho, T. Aho, R. Isoaho, A. Tukiainen, M. Guina, *Sol. Energy Mater. Sol. Cells* **2021**, *226*, 111097.
- [38] S. Pouladi, C. Favela, W. Wang, M. Moradnia, N.-I. Kim, S. Shervin, J. Chen, S. Sharma, G. Yang, M.-C. Nguyen, R. Choi, J. Kim, A. Fedorenko, B. Bogner, J. Bao, S. M. Hubbard, V. Selvamanickam, J.-H. Ryou, *Sol. Energy Mater. Sol. Cells* **2022**, *243*, 111791.